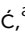


Cite this: *Chem. Sci.*, 2023, 14, 9389 All publication charges for this article have been paid for by the Royal Society of Chemistry

# Improving the molecular spin qubit performance in zirconium MOF composites by mechanochemical dilution and fullerene encapsulation†

Lucija Vujević,<sup>a</sup> Bahar Karadeniz,<sup>a</sup> \*<sup>a</sup> Nikola Cindro,<sup>b</sup> <sup>b</sup> Andraž Krajnc,<sup>c</sup> Gregor Mali,<sup>c</sup> <sup>c</sup> Matjaž Mazaj,<sup>c</sup> <sup>c</sup> Stanislav M. Avdoshenko,<sup>d</sup> Alexey A. Popov,<sup>d</sup> <sup>d</sup> Dijana Žilić,<sup>b</sup> \*<sup>a</sup> Krunoslav Užarević,<sup>b</sup> \*<sup>a</sup> and Marina Kveder\*<sup>a</sup>

Enlarging the quantum coherence times and gaining control over quantum effects in real systems are fundamental for developing quantum technologies. Molecular electron spin qubits are particularly promising candidates for realizing quantum information processing due to their modularity and tunability. Still, there is a constant search for tools to increase their quantum coherence times. Here we present how the mechanochemical introduction of active spin qubits in the form of 10% diluted copper(II)-porphyrins in the diamagnetic PCN-223 and MOF-525 zirconium-MOF polymorph pair can be achieved. Furthermore, the encapsulation of fullerene during the MOF synthesis directs the process exclusively toward the rare PCN-223 framework with a controllable amount of fullerene in the framework channels. In addition to the templating role, the incorporation of fullerene increases the electron spin–lattice and phase-memory relaxation times,  $T_1$  and  $T_m$ . Besides decreasing the amount of nuclear spin-bearing solvent guests in the non-activated qubit frameworks, the observed improved relaxation times can be rationalized by modulating the phonon density of states upon fullerene encapsulation.

Received 16th June 2023  
Accepted 12th August 2023

DOI: 10.1039/d3sc03089j

rsc.li/chemical-science

## 1 Introduction

A fundamental step towards developing of quantum technologies is building a qubit, a quantum bit that can exist in a coherent superposition state, unlike the classical bit that can possess only two states, 0 and 1.<sup>1</sup> Among different ways of qubit realization, electron spin in molecular magnetic compounds, where the spin originates from the organic radical, transition metal ion or lanthanide, is particularly promising technology due to the facile manipulation of the electron quantum states by an electromagnetic irradiation.<sup>2,3</sup> The main prerequisite for building a quantum device is the entanglement of qubits to achieve a state that is not the simple product of individual qubits. The inclusion of molecular spin qubits into the specifically tailored environment enables the study of the effect of spatial separation and interactions within the framework on the qubit performance, unraveling the role of phonon environment and spin–spin interactions on the operating speed of the qubit

(spin–lattice relaxation time rate,  $1/T_1$ ) and on the time limit in which the computation must be performed (phase-memory time,  $T_m$ ).<sup>4</sup> Much effort is put into suppressing various origins of spin decoherence, such as due to the framework noise and interaction with nearby nuclei.<sup>5</sup> To fully realize the potential of molecular spins for quantum information processing, it is necessary to build structurally well-defined arrays of spatially resolved molecular spins, hence combining improved spin coherence properties with optical or electrical access to their quantum states.<sup>5–7</sup>

Metal–organic frameworks (MOFs)<sup>8,9</sup> assert as an ideal platform for controllable spatial resolution of qubit sites.<sup>4,10</sup> These coordination polymers combine the coordination preferences of the metal cation nodes with different geometry of organic linkers to form a plethora of diverse topologies characterized by permanent porosity, different nature of the interior walls, and approachable metal nodes, not only on the surface but also in the interior of MOF particles. The modularity and tunability of MOFs, particularly MOFs of the fourth generation, made them one of the most investigated material classes today, with many potential application areas.<sup>11,12</sup> In terms of quantum technologies, the variable topologies, periodicity, chemical diversity, and high internal ordering of MOFs provide an ideal and tunable platform for spatial resolution and manipulation of molecular spins, leading towards an emerging class of 3D-qubit array materials.<sup>4</sup> Building such a MOF platform with long coherence

<sup>a</sup>Ruđer Bošković Institute, Bijenička cesta 54, 10000 Zagreb, Croatia. E-mail: bahar.karadeniz@irb.hr; dijana.zilic@irb.hr; krunoslav.uzarevic@irb.hr; kveder@irb.hr<sup>b</sup>Department of Chemistry, University of Zagreb, 10000 Zagreb, Croatia<sup>c</sup>National Institute of Chemistry, Hajdrihova 19, SI-1001 Ljubljana, Slovenia<sup>d</sup>Leibniz IFW Dresden, Helmholtzstrasse 20, D-01069 Dresden, Germany† Electronic supplementary information (ESI) available: Experimental and additional characterization. See DOI: <https://doi.org/10.1039/d3sc03089j>

time is a demanding task as the spin carriers need to be sufficiently separated from each other, while it is still not possible to maintain spatial precision at a molecular level in MOFs with highly diluted spin carriers. Also, MOFs inherently carry the magnetic noise of the ligands and guest molecules in the matrix, which may lead to the decoherence of qubits and usually shorter qubit lifetimes than required for quantum information processing (QIP) or quantum sensing.<sup>13,14</sup> Most of these issues are, however, amendable, and it has been reported that including the copper(II)-porphyrin building blocks in highly porous and activated MOFs results in spin coherence detectable up to liquid-nitrogen temperatures, making these materials attractive from the perspective of quantum information science.<sup>4</sup> Therefore, understanding quantum system interactions with its respective environment plays a key step in controlling decoherence processes expressed in terms of  $T_1$  and  $T_m$  (an approximation of spin–spin relaxation time  $T_2$ ) relaxation times.<sup>15</sup>

A promising class of MOFs for quantum computing are porphyrinic zirconium carboxylate MOFs built from tetrapopic porphyrinic ligand, tetrakis(4-carboxyphenyl)porphyrin ( $H_2$ TCPP), and hexanuclear or octanuclear oxozirconium(IV) clusters.<sup>16,17</sup> Zirconium carboxylate MOFs<sup>18</sup> are widely researched due to their resistance to water and corrosive atmospheres,<sup>19,20</sup> and framework-stability upon linker removal, leading to increased porosity of the material and larger distancing between the spin carriers.<sup>21,22</sup> Despite zirconium(IV) clusters and resulting MOFs being diamagnetic, the spin active atom or group can be coordinated in the porphyrin center and efficiently separated by the coordination of the metalloporphyrin with binding carboxylate groups in the MOF structure.<sup>23</sup> Porphyrin MOFs are rare zirconium MOFs displaying more than one topology.<sup>24</sup> For some of the six known topologies, a polymorphic transition is also possible, for example, in the case of MOF-525 and PCN-223 polymorph pair (Fig. 1).<sup>25</sup> Freedman's group, in their recent proof-of-concept work, exploited cobalt(II) porphyrin molecular magnets diluted in a highly porous hexa-coordinated (on the zirconium cluster) PCN-224 MOF<sup>17</sup> matrix for accomplishing a porous array of clocklike qubits, to tackle the issue with magnetic noise of the nuclear-spins rich MOF carrier.<sup>26</sup> The same group showed how the incorporation of spin-active copper(II) porphyrins into the PCN-224 results in porous molecular spin-based qubits with detectable coherence among the highly-concentrated spins in the framework up to 80 K (Fig. 1).<sup>4,27</sup> In this context, copper(II) porphyrins, where the copper bears  $S = 1/2$  electronic spin, became attractive and extensively studied model systems for quantum information processing applications. The coherence parameters in terms of  $T_1$  and  $T_m$  were investigated using pulse ESR spectroscopy in addition to continuous wave (CW)-ESR.<sup>10,23,28</sup> Not only the molecular spin-based qubits with high porosity and missing linkers, such as PCN-224, are suitable molecular spin qubit candidates. In our recent work, we showed how mechanochemistry<sup>29</sup> provides a controllable pathway to synthesizing phase-pure twelve-coordinated PCN-223 and MOF-525 polymorphs.<sup>25</sup> By introducing paramagnetic centers (Cu(II), Fe(III), and Mn(II)) in the porphyrin linker, a superhyperfine

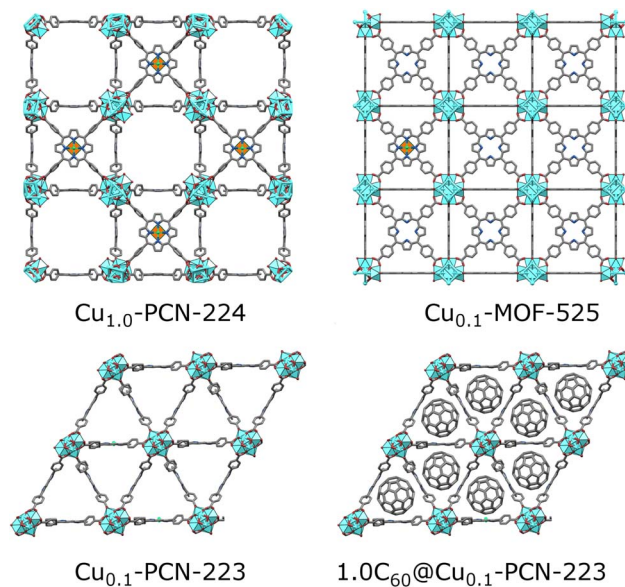


Fig. 1 Porphyrinic Zr-MOFs considered for quantum information processing application; six-coordinated PCN-224 with a low population of linkers allowed for dense Cu(II) spin-arrays (orange-green polyhedra in the center of porphyrin moiety).<sup>4</sup> MOF-525 and PCN-223 involved in this study are twelve-coordinated, with a dense population of mixed TCPP linkers involving 10 percent of Cu(II)-TCPP, which may lead to better stability of materials. The introduction of fullerene steers the formation exclusively towards the PCN-223 framework, with the fullerene populating the voids of the MOF.

splitting was observed in CW-ESR spectra of the more porous MOF-525 polymorph. In contrast, the same feature was less pronounced in PCN-223 where the nearest distance between the paramagnetic centers is 1.07 nm.<sup>25</sup> The observed phenomenon denoted these materials as potential candidates for applications in quantum information processing.

An interesting strategy for manipulating the coherence among the spin carriers in framework materials is an introduction of guests that influence the framework properties and affect the height of the energy barrier, which may positively influence the  $T_1$ -relaxation time.<sup>30,31</sup> Our recent work showed that the introduction of  $C_{60}$  fullerene to sodalite ZIF-8 framework resulted in the stiffening of the framework and increased resistance to electromagnetic radiation, which depended on the ratio of the encapsulated fullerene.<sup>32</sup> Here, we choose fullerene as an almost nuclear spin-free to reduce spin pollution, possibly increase the rigidity of the framework, and influence  $T_m$ . The fullerene as a solid guest was also chosen to avoid a need for frozen  $CS_2$  suspensions as reported by Freedman's group<sup>13</sup> or challenges related to the activation and removal of spin-pollutants in MOFs.<sup>33</sup>

Here, the presented study focuses on the modulation of copper(II)-porphyrin qubit properties in the MOF-525 and PCN-223 polymorphic pair by diluting the spin carriers in the MOF structure and encapsulating the fullerene in the cavities of these spin-active frameworks. Whereas the proper distancing of the spin centers in MOFs is a well-known prerequisite for establishing coherence among the molecular spin carriers, where the



MOF-525 showed to be advantageous, we are particularly interested to see how the controllable incorporation<sup>32</sup> of a nanosized functional guest such as C<sub>60</sub> fullerene within the channels of formed molecular spin-based qubit will be reflected on the coherence of the spin arrays in the robust and non-activated MOF samples.<sup>34</sup>

While previously MOF-525 was the predominant product of solution and mechanochemical syntheses,<sup>25</sup> the introduction of fullerene inverts the selectivity of framework formation towards rarer PCN-223 polymorph, with the fullerene serving as a template and residing in triangular channels along the crystallographic *c* axis (Fig. S2†). For this study, we also prepared two fulleretic molecular spin-based qubits PCN-223 frameworks with different amounts of encapsulated C<sub>60</sub> fullerene. The CW-ESR spectra analyses unravel magneto-structural characteristics of the copper-porphyrin qubit environment, including the local symmetry of the copper center in terms of *g* and hyperfine *A* tensors for both diluted molecular spin-based qubits. Besides direct measuring of spin-relaxation times, other pulsed ESR experiments were performed, such as HYSORE and Rabi oscillations, to gain relevant information about the interactions with the environment's nuclei. The experimental and theoretical results point towards the multifunctional role of the fullerene for the prolongation of coherence times among the spin carriers, involving the reduction of spin noise and altering the spin-phonon interactions.

## 2 Results and discussion

Synthesis, DFT, IR, solid-state NMR, and CW/pulse ESR studies of 12-connected porphyritic zirconium MOF polymorphs, Cu-MOF-525 (cubic, ftw), Cu-PCN-223 (hexagonal, shp) and their composites, are presented. The copper(II) ratio in the porphyrin centers of the synthesized MOFs was diluted to 10% copper(II) as the copper(II)–copper(II) interactions cause line broadening in CW-ESR and destroy electron spin coherence in pulse ESR.

### 2.1 Synthesis

Our group recently reported the synthesis and controlled topology transformation of metallated and metal-free MOF-525 and PCN-223 by mechanochemistry.<sup>25</sup> The here investigated multivariate Cu<sub>0.1</sub>-MOF-525 and Cu<sub>0.1</sub>-PCN-223 frameworks were synthesized in the same manner, with the difference that the CuTCCP and H<sub>2</sub>TCCP ligands were milled together in the desired ratio before the introduction of the zirconium source and the MOF formation, to ensure the homogeneous distribution of the diluted CuTCCP in the framework. The mechanochemical formation reactions are almost quantitative, yielding the insoluble MOF product without other H<sub>2</sub>TCCP byproducts observable in the PXRD of the crude product. The washing of the product is colorless, which further points towards the high efficiency of these reactions (the H<sub>2</sub>TCCP gives highly colored solutions even in low concentrations). A controlled amount of fullerene C<sub>60</sub> (20 and 100 mol%) was successfully encapsulated into Cu<sub>0.1</sub>-PCN-223 using the one-pot liquid-assisted grinding (LAG) MOF formation.<sup>32</sup> Noteworthy, in our previous work, the

MOF-525 was predominant product, and PCN-223 polymorph could be obtained only in specific reaction conditions.<sup>25</sup>

Interestingly, the presence of C<sub>60</sub> in the reaction mixture drives the formation exclusively towards hexagonal shp-C<sub>60</sub>@Cu<sub>0.1</sub>-PCN-223 polymorph, even with the reaction conditions that would in all cases afford the cubic ftw-Cu<sub>0.1</sub>-MOF-525 phase.<sup>25</sup> C<sub>60</sub> thus acted as a template providing the C<sub>60</sub>@Cu<sub>0.1</sub>-PCN-223 composite, and no traces of MOF-525 have been detected in any product. Tentatively, the arrangement of the linkers and channel size of PCN-223 polymorph is more suitable for encapsulating C<sub>60</sub>. While the similar templating effect of C<sub>60</sub> has been reported previously on tuning the cavity size of multiporphyrin macrocycles,<sup>35</sup> no similar effect has been, to the best of our knowledge, reported for any zirconium carboxylate framework. The washing of the crude milling product was almost colorless, indicating, together with the FTIR and PXRD analyses, that the C<sub>60</sub> guest was included in the pores of the frameworks in its entirety. After the C<sub>60</sub> capture, DMF is still present in the pores of the products, but in a lower amount than in the non-fulleretic analogs (Fig. S3†). The PCN-223 structure has voids along the crystallographic *a*-axis that are too narrow for the accommodation of C<sub>60</sub>, but suitable for smaller DMF molecules (Fig. S2†).

Synthesized MOFs and MOF composites are phase-pure and highly crystalline, and no free fullerene is visible in products after washing (Fig. 2). The disappearance of C<sub>60</sub> peaks in the PXRD patterns confirms the absence of C<sub>60</sub> crystals on the surface of MOF composites. PXRD data also provide a qualitative measure of the encapsulation of C<sub>60</sub> within the PCN-223 framework. The intensity of the low angle peak, 2θ = 4.80, decreases due to the modified electron density in the MOF cage as a result of loading C<sub>60</sub> in the channels of PCN-223

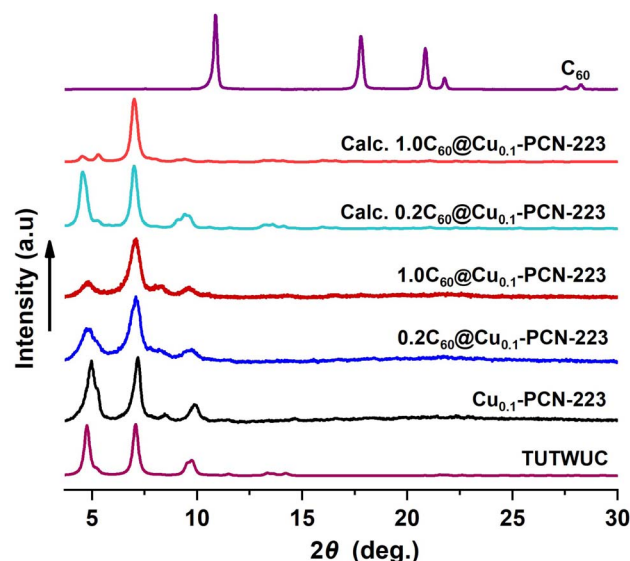


Fig. 2 PXRD data for Cu<sub>0.1</sub>-PCN-223 and the C<sub>60</sub>@Cu<sub>0.1</sub>-PCN-223 composites vs. PXRD data for PCN-223 simulated from the single crystal diffraction data (Cambridge Crystallographic Data Centre (CCDC) code: TUTWUC) and two fulleretic composites optimized in this study (please see Section 2.2).



framework,<sup>32,36</sup> which is also corroborated here by DFT. Calculated PXRD data closely matched the experimentally observed PXRD data, supporting the reduction of the low-angle peak intensity (Fig. 2), which is the effect of guest inclusion into the cage, similar to the previously observed behavior in fulleretic ZIF-8 hybrids.<sup>32</sup> The weak Bragg reflection occurring in the fulleretic MOFs derived from the DFT study (please see Section 2.2) and not clearly visible in experimental data is likely due to the fullerene being fixed in one position, while the spectroscopic and computational studies suggest it to be heavily rotationally disordered.

Due to hard-to-control defects in the MOF structures and the dynamic nature of the MOF pore content that can exchange with the atmosphere, the analysis of MOFs composition is a demanding task, which is, for example, best visible in the problems related to the determination of one of the most researched and essential features of MOFs, their porosity.<sup>37</sup> Zirconia porphyrin MOFs are not an exemption, showing up to 40% of missing linker defects without the collapse of the MOF structure.<sup>38</sup> For the samples prepared in this work, the elemental analysis showed missing linkers defects in all products, an increase in carbon content, and a decrease in the hydrogen and nitrogen content after the encapsulation of fullerene. Here however, we primarily aimed to determine the ratio of copper to zirconium to establish whether the targeted implementation of the 10% of copper(II) spin carriers to the framework was successful since the variation in copper(II) content can affect the  $T_m$ . To quantify the Cu/Zr ratio in the studied multivariate MOFs and establish the  $C_{60}$  content in their pores, we performed inductively coupled plasma mass spectrometry (ICP-MS) and energy dispersive X-ray spectroscopy on a Cs-probe corrected transmission electron microscope (EDAX-TEM) analyses (Fig. S1†).

ICP-MS data found the molar ratio of Zr(IV) : Cu(II) to be 18 : 1 for  $C_{60}@Cu_{0.1}$ -PCN-223 (20 : 1 estimated), 1.92 : 1 for  $C_{60}@Cu_{1.0}$ -PCN-223 (2 : 1 estimated), and 20 : 1 for fullerene-free  $Cu_{0.1}$ -MOF-525 (20 : 1 estimated). The analysis showed *ca.* 10-fold lower quantity of Cu(II) spin carriers in the framework with diluted Cu(II) spin carriers,  $C_{60}@Cu_{0.1}$ -PCN-223. Also, the absolute values of Zr(IV) and Cu(II) in the fulleretic frameworks confirmed the high loading of  $C_{60}$  in the framework, as can be seen by the differences in the Zr(IV) and Cu(II) content established for  $C_{60}$  encapsulated and  $C_{60}$ -free MOF frameworks (ESI, Materials and methods†). The deviations from the idealized formulae may be due to the defects in structure and variable content of guests in the framework that we could not remove from the framework by standard activation procedures. EDAX-TEM showed homogeneous distribution of copper(II) spin carriers in both fulleretic phases, the  $C_{60}@Cu_{0.1}$ -PCN-223 and  $C_{60}@Cu_{1.0}$ -PCN-223 (ESI, Fig. S1†). The relative molar ratio of the Zr/Cu in these samples corresponds well to the ICP-MS analysis, being approximately ten times higher for  $C_{60}@Cu_{0.1}$ -PCN-223 than the Zr/Cu for  $C_{60}@Cu_{1.0}$ -PCN-223. The absolute values and the carbon content in the frameworks were not possible to estimate by this method due to the samples being collected at the carbon foil influencing the measurement.

We can conclude from these analyses that the mechanochemical formation provided MOFs with the desired ratio of Cu-spin carriers in the framework and the homogeneous distribution at the TEM resolution. It must be noted that we could not completely control the distribution of the CuTCPP in the framework at a molecular level. As in other materials with diluted active spin carriers (for example, defects in nanodiamonds), the controllable implementation of diluted active species to MOFs is still a complex and hard-to-achieve issue. It is possible in some specific cases, for example, when the ligands have different binding functionalities, as in the case of bimetallic MOF-74 formation.<sup>29,39</sup> Here, however, Cu-TCPP and  $H_2$ TCPP have the same binding functionalities and affinity towards zirconium-MOF formation, so their implementation to the framework is largely stochastic. Regardless, the ESR analyses showed efficient separation of copper centers in the formed multivariate MOFs (please see section CW-ESR spectroscopy below).

## 2.2 DFT study

The system size allows a comprehensive DFT study (DFT/PAW/PBE-D, see ESI† for computational details) of the stability and dynamics of the PCN-223 framework with  $C_{60}$  molecules inside. The PCN-223 framework is relatively spacious, and after full optimization, no significant change in the C-C bond parameters of the  $C_{60}$  fullerene itself could be observed. The calculations also reveal a lack of significant affinity of the fullerene molecules toward the MOF framework, and the  $C_{60}$  molecules tend to stay in the middle of the voids.

Within the channel, molecules appear to be well isolated from other parallel channels, although the distance between the closest molecules from the adjacent channels is roughly 6 Å (Fig. S2†). At the same time, the distance between the  $C_{60}$  molecules within a single channel is 8 Å, which undermines the possibility of significant electronic interaction between them. High-density fillings would be required to provide significant intermolecular interaction among the fullerenes within the channel. Further investigation of the system using the DFTB/MD method reveals that molecules can freely rotate on-site (Fig. 3a). Fig. 3a shows the time-averaged trajectory of the carbon cage atoms along the 100 picosecond trajectory while the vibrational densities of states are shown in Fig. 3b. The

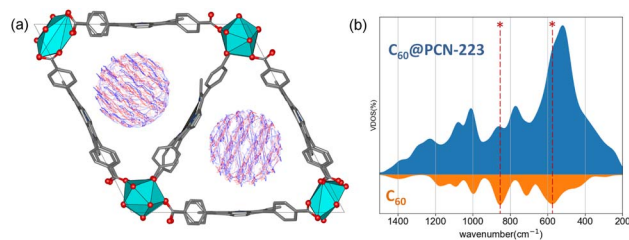


Fig. 3 (a) Superposition of time-averaged snapshots for  $C_{60}$  within a 100 ps time-window of  $C_{60}@PCN-223$  dynamics at DFTB level of theory. (b) MD recovered the total and projected vibrational density of states for  $C_{60}@PCN-223$  and  $C_{60}$ , where asterisks mark the most profound contribution by  $C_{60}$  in the total VDOS.



time-averaging smooths out continuous molecular motion along with the principal components of rotations. Within the channel, such a rotation would undoubtedly lead to a sizeable disorder. The aforementioned dense packing might partially prevent intense rotations.

### 2.3 FTIR-ATR spectroscopy

FTIR-ATR data of  $\text{Cu}_{0.1}$ -MOF-525,  $\text{Cu}_{0.1}$ -PCN-223, and (20% and 100%),  $\text{C}_{60}$ @ $\text{Cu}_{0.1}$ -PCN-223 are consistent with their counterparts in the literature.<sup>25</sup> The appearance of a new vibrational peak at  $526\text{ cm}^{-1}$  with a slight shift in the spectrum of (20% and 100%)  $\text{C}_{60}$ @ $\text{Cu}_{0.1}$ -PCN-223 is clearly assigned to the most dominant vibration signal of pristine  $\text{C}_{60}$ , at  $523\text{ cm}^{-1}$ , proving the incorporation of  $\text{C}_{60}$  into the framework while the other vibration peaks of pristine  $\text{C}_{60}$  overlap with the framework features (Fig. S3†). The FTIR data reveals the presence of formamide solvent in the framework.

### 2.4 NMR spectroscopy

The results of solid-state NMR spectroscopy are presented in Fig. 4. Peak assignment was performed from the analysis of CPMAS and HETCOR spectra (Fig. S4 and S5†). The signal of  $^{13}\text{C}$  nuclei of  $\text{C}_{60}$  in the  $\text{C}_{60}$ @ $\text{Cu}_{0.1}$ -PCN-223, appearing at *ca.* 138 ppm, is narrow, suggesting that fullerene is free-standing and rotating inside the MOF channels. Any stronger

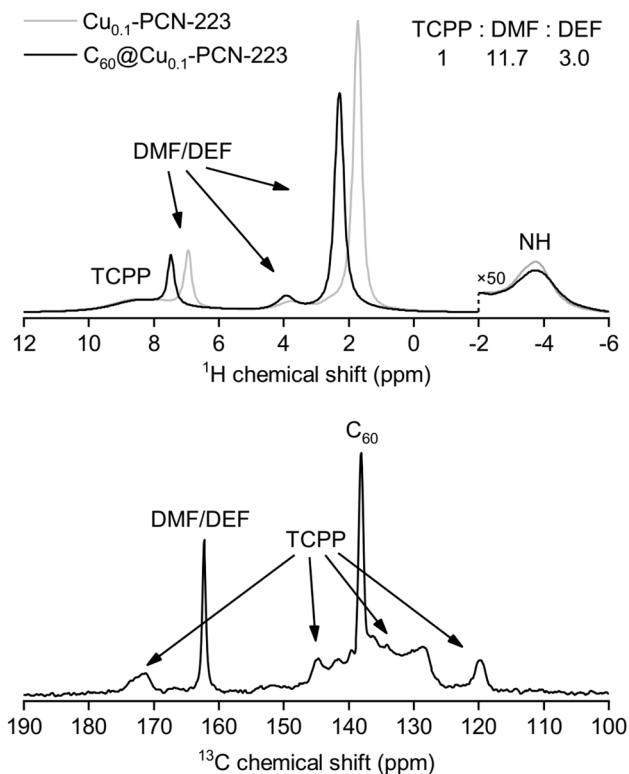


Fig. 4 (Up)  $^1\text{H}$  MAS NMR spectra for  $\text{Cu}_{0.1}$ -PCN-223 and  $1.0\text{C}_{60}$ @ $\text{Cu}_{0.1}$ -PCN-223 at 300 K. (Down)  $^{13}\text{C}$  MAS NMR spectrum of  $1.0\text{C}_{60}$ @ $\text{Cu}_{0.1}$ -PCN-223 at 300 K. The signals from dimethylformamide (DMF), diethylformamide (DEF),  $\text{H}_2$ TCPP linker and fullerene ( $\text{C}_{60}$ ) are indicated on the spectra.

anisotropic interaction with proximal paramagnetic copper centers is thus motionally averaged out. In the sodalite zeolitic-imidazolate-framework-8, fullerene was completely immobilized in the discrete voids of the framework, and its inclusion led to the stiffening of the framework.<sup>32</sup> Here, the  $^{13}\text{C}$  MAS NMR spectra of  $\text{C}_{60}$ @ $\text{Cu}_{0.1}$ -PCN-223 in the region between 125 ppm and 135 ppm, and at about 145 ppm show that the incorporation of  $\text{C}_{60}$  to the PCN-223 framework leads to small shifts in the TCPP signal position, but it is hard to determine the precise effect of the  $\text{C}_{60}$  inclusion on the framework properties.  $^1\text{H}$  and  $^{13}\text{C}$  MAS recorded for  $1.0\text{C}_{60}$ @ $\text{Cu}_{0.1}$ -PCN-223 corroborate that the DMF and DEF used for washing and aging are still present within the pores of the network. Moreover, the downfield shifts of the  $^1\text{H}$  signals suggest that the formamide molecules are either brought closer to the porphyrin rings upon  $\text{C}_{60}$  encapsulation or experience a reduced chemical shift averaging effect due to their motion being impeded by the encapsulated fullerenes.<sup>40</sup>

### 2.5 CW-ESR spectroscopy

CW-ESR spectra of various MOFs recorded at 40 K showing axial symmetry are presented in Fig. 5. It can be noticed that both  $\text{Cu}_{0.1}$ -MOF-525 and  $\text{Cu}_{0.1}$ -PCN-223 exhibit typical CW-ESR spectra of the diluted copper porphyrin monomers (Fig. 5a).<sup>28,41</sup> The strong hyperfine coupling of the unpaired electron spin with the copper nuclear magnetic moment ( $I = 3/2$ ) results in four lines, three of which are resolved in the low-field part of the spectrum. In comparison with the previously reported ESR spectra, which did not reflect the interaction with four nitrogen atoms from the porphyrin macrocycle in the first derivation of the absorption ESR spectra due to the high copper concentration (100% Cu,  $\text{Cu}_{1.0}$ -PCN-223),<sup>25</sup> here presented data exhibit strong modulation of the high-field part of the spectrum (Fig. 5a). This superhyperfine interaction in the ESR spectra of a sample with a lower

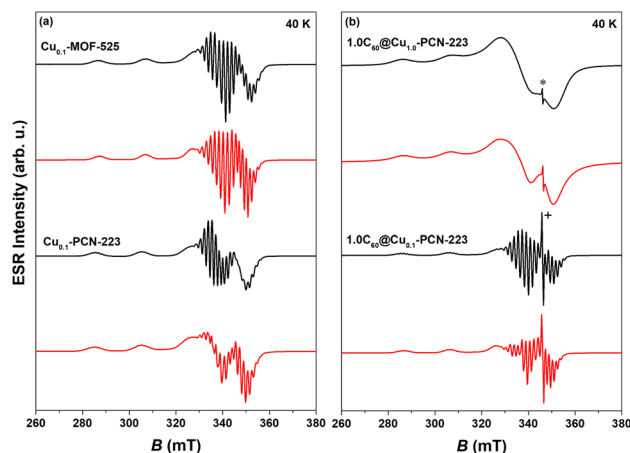


Fig. 5 Experimental (black) and simulated CW-ESR spectra (red) of various MOFs recorded at 40 K: (a)  $\text{Cu}_{0.1}$ -MOF-525 and  $\text{Cu}_{0.1}$ -PCN-223, (b)  $1.0\text{C}_{60}$ @ $\text{Cu}_{0.1}$ -PCN-223 and  $1.0\text{C}_{60}$ @ $\text{Cu}_{0.1}$ -PCN-223. Asterisk in the figure indicates the fullerene-radical (FR) signal at  $g \approx 2.003$  while "+" denotes truncation of the peak. Parameters of the simulated spectra are reported in Table S1.†



concentration of copper ions (10% Cu) provides evidence of the capability of mechanochemical procedures to dilute metal ions in the molecular framework in a largely controllable manner.

The experimental spectra were simulated using EasySpin software<sup>42</sup> assuming axial symmetry of  $g$  tensor and  $A$  hyperfine tensor while all four nitrogen atoms in the porphyrin ring were assumed to be equivalent.<sup>43</sup> In specific, the tensor components  $g_{\parallel}$  and  $A_{\parallel}$  correspond to the orientation perpendicular to the porphyrin plane while  $g_{\perp}$  and  $A_{\perp}$  represent planar, plane orientation.<sup>4</sup> In the interaction of the copper electron spin ( $S = 1/2$ ) with the copper nucleus spin ( $I_{\text{Cu}} = 3/2$ ) the same hyperfine coupling for natural-abundance mixture of copper isotopes (<sup>63</sup>Cu and <sup>65</sup>Cu) was assumed.<sup>41</sup> Therefore, the following spin-Hamiltonian for copper electron spin was used:

$$H_{\text{Cu}} = \mu_{\text{B}}BgS + SA_{\text{Cu}}I_{\text{Cu}} + SA_{\text{N}}I_{\text{N}} \quad (1)$$

where  $B$  is external magnetic field while the constant  $\mu_{\text{B}}$  is Bohr magneton. The parameters obtained from the simulations are given in Table S1† and are consistent with the data reported in the literature.<sup>44</sup> In specific, the spectra exhibit  $g_{\parallel} > g_{\perp} > g_{\text{e}}$  indicative of the  $d_{x^2-y^2}$  copper electron spin ground state. No essential difference of  $g$ -tensor values in Cu<sub>0.1</sub>-PCN-223 and Cu<sub>0.1</sub>-MOF-525 indicates no difference in their respective orbital angular momentum contributions. Similarly, hyperfine/superhyperfine tensor differences are within the experimental variability of data. In addition, the tetrahedral distortion of the square planar copper geometry<sup>45</sup> estimated from the ratio  $f = g_{\parallel}/A_{\parallel}^{\text{Cu}}$  indicates perfect square-planar geometry which pertains upon the incorporation of fullerene (Table S2†). The corresponding CW-ESR spectra of 1.0C<sub>60</sub>@Cu<sub>1.0</sub>-PCN-223 and 1.0C<sub>60</sub>@Cu<sub>0.1</sub>-PCN-223 are presented in Fig. 5b. Fullerene has a weak ESR signal (FR) at  $g_{\text{FR}} \approx 2.002$  due to defects in fullerene structure (Fig. S21† in ESI in ref. 32). This signal is even visible when the structure was loaded with 100% of Cu although the superhyperfine lines could not be resolved due to strong spin-spin interactions between copper cations (Fig. 5b). Additionally, there is a signal of empty H<sub>2</sub>TCPP (without copper ions in porphyrin rings) at a similar  $g$ -value as the fullerene-radical signal but this signal is broader, weaker, and suppressed by the stronger FR signals. Due to this fact, the simulation of the experimental spectra was done in terms of a mixture of spin species by combining the spin-Hamiltonian of copper given by eqn (1) and spin-Hamiltonian of FR while assuming  $S_{\text{FR}} = 1/2$ :  $H_{\text{FR}} = \mu_{\text{B}}Bg_{\text{FR}}S_{\text{FR}}$ . As C<sub>60</sub> is known to be a good electron acceptor, and porphyrins are also electroactive, an electron transfer between the fullerene and porphyrin linkers in MOFs may occur. However, based on their respective redox potential, this possibility is unlikely.<sup>46,47</sup>

The simulation parameters<sup>42</sup> and the corresponding spectra are given in Table S1† and Fig. 5b. The obtained data are in accordance with the NMR and DFT studies and the literature stating that encapsulated fullerene is free-standing inside the cage.<sup>32</sup>

## 2.6 Pulse ESR spectroscopy

Two-pulse echo detected field-swept ESR spectra of various MOFs were recorded at 80 K in order to assign the spectral

positions for relaxation time measurements in pulsed ESR experiments (Fig. 6a). Two Cu(II) magnetic field resonances were chosen, which correspond to two principles  $g$ -tensor values  $g_{\parallel} = 2.2$  and  $g_{\perp} = 2.06$ .<sup>4</sup>

**2.6.1 Spin-lattice relaxation time.** The electron spin-lattice relaxation times,  $T_1$ , of four MOF-samples: Cu<sub>0.1</sub>-PCN-223, 0.2C<sub>60</sub>@Cu<sub>0.1</sub>-PCN-223, 1.0C<sub>60</sub>@Cu<sub>0.1</sub>-PCN-223 as well as of Cu<sub>0.1</sub>-MOF-525 were measured across temperature range of 5–80 K (Fig. S7†). The shortest  $T_1$  was detected for Cu<sub>0.1</sub>-PCN-223, which, upon loading of the fullerene molecules into the structure, presented much longer  $T_1$  values (Fig. 6b). This phenomenon can be noticed in the whole temperature range studied. In specific, the longest  $T_1$  of ca. 6.7 (5.3) ms was measured at 5 K and  $g_{\parallel}$  position for 0.2C<sub>60</sub>@Cu<sub>0.1</sub>-PCN-223 (1.0C<sub>60</sub>@Cu<sub>0.1</sub>-PCN-223) as compared with the empty Cu<sub>0.1</sub>-PCN-223 which exhibited  $T_1$  of ca. 3.5 ms. After heating the samples to 80 K,  $T_1$  values decreased by three orders of magnitude and converged to similar  $T_1$  values in the range of 5  $\mu$ s (Fig. 6b). For all the samples studied,  $T_1$  measured at  $g_{\parallel}$  was longer than the one at  $g_{\perp}$  position by a factor of two at the lowest temperatures studied (Fig. S7†). Interestingly, at the lowest temperatures studied  $T_1$  values of MOF-525 were similar to the values of PCN-223 loaded with fullerene while approaching the similar values of other MOFs upon heating up the sample (Fig. S7†).  $T_1$  data obtained here show one order-of-magnitude longer values at the lowest temperatures compared with data for copper-porphyrin qubits in Cu<sub>0.1</sub>-PCN-224 (ref. 4) and Zr-Cu-NU-1102 (ref. 27) while has the same order-of-magnitude values compared to the data for copper-porphyrin qubits in 2D nanosheets.<sup>23</sup>

The fullerene encapsulation alters the phonon density of states of the material, affecting thus relaxation times. To understand the experimental data, various mechanisms transferring the spin excitation energy to the crystal lattice were considered. Since no thermally accessible electronic excited states are expected for copper(II) complexes, the Orbach-Aminov mechanism was neglected.<sup>48,49</sup> Finally, three main processes of the spin-lattice relaxation rate,  $1/T_1$ , were assigned to adequately reproduce the experimental data: direct one-phonon, two-phonon Raman, and local mode-mediated processes.<sup>48</sup> In this context, assuming the Debye type of phonon spectrum, experimental  $1/T_1$  values were fitted according to equation<sup>48,50</sup>

$$1/T_1 = aT + b \frac{T^9}{\theta^7} J_8 + c \frac{e^{A/T}}{(e^{A/T} - 1)^2}, \quad (2)$$

as shown in Fig. 6b while the best-fit parameters are given in Table 1 and with more statistical details in Table S3.† It should be stressed that due to the problem of reaching the global minimum in non-linear fitting with 5 unknown parameters, the obtained values here should be considered as an estimation of the possible parameters rather than the unique solutions. The first term describes the one-phonon process, and it is important at the lowest temperatures studied when the phonons with high energy are still not excited. The second term is related to the two-phonon Raman process with  $J_8$  denoting the transport integral, which was solved numerically, while  $\theta$  is Debye





Fig. 6 (a) Experimental (black) and simulated (red) two-pulse echo detected field-swept ESR spectrum of  $\text{Cu}_{0.1}\text{-PCN-223}$  recorded at  $T = 80$  K. The tensor values  $g_{\parallel} = 2.2$  and  $g_{\perp} = 2.06$  labeled by arrows indicate the magnetic field spectral positions at which spin dynamics was undertaken. (b) Temperature dependence of the electron spin–lattice relaxation rate,  $1/T_1$ , of  $\text{Cu}_{0.1}\text{-PCN-223}$  (black),  $0.2\text{C}_{60}@Cu_{0.1}\text{-PCN-223}$  (blue) and  $1.0\text{C}_{60}@Cu_{0.1}\text{-PCN-223}$  (red) measured at  $g_{\parallel}$  spectral position. Full lines denote best-fits of the experimental data according to the eqn (2) with the parameters given in Table 1. In the inset to the figure, magnetization recovery curves are given in the inversion recovery experiment detected at 5 K. (c) Temperature dependence of the electron-spin phase-memory relaxation time,  $T_m$ , in various MOFs at  $g_{\parallel}$  spectral position.

temperature. The last term describes local-mode mediated process of energy  $\Delta$ .<sup>48,51</sup> The example of various terms contribution is illustrated in Fig. S8.†

The results of the fitting presented in Table 1 clearly show that the anisotropy of  $T_1$  regarding the spectral positions of  $g_{\parallel}$  and  $g_{\perp}$  is present in all the samples studied. The analogous anisotropy of  $T_1$  data was reported for similar copper porphyrin structures in PCN-224.<sup>4,27</sup> Along with the seminal work presented by Eaton's group,<sup>52</sup> the very recent work by Kazmierczak and Hadt<sup>53</sup> has investigated both experimentally and theoretically a library of Cu(II) and V(IV) complexes exhibiting comparable  $T_1$  anisotropy. A theory based on the spin–orbit coupling wave functions and different ligand field contributions at two  $g$ -positions successfully reproduced inversion recovery measurements performed at 100 K. It is interesting to note that here observed anisotropy of  $T_1$  (Table 1) is most visible in the region of lowest temperatures studied where the direct process is governing the electron spin relaxation.

Additionally, Table 1 shows two main differences between MOF samples with and without fullerene. First, the samples containing fullerene exhibit a smaller value of parameter  $a$  than those without fullerene, implying a slowing down of the direct process. Second, related to the Raman process, a considerable trend in Debye temperature towards higher values in the presence of fullerene can be noticed despite large uncertainties of

the fitted values. The larger Debye temperature might be related to the combined effect of the increased number of oscillators and the speed of sound upon fullerene incorporation in MOF matrix.<sup>54</sup> The values for Debye temperatures obtained here have the same order of magnitude as the value of 102 K found for MOF-5.<sup>55</sup> Regarding the local-mode mediated process, energy values of  $\Delta \approx 280$  K ( $200\text{ cm}^{-1}$ ) were obtained (Table 1). This value is too high for the acoustic phonons to be involved, while it is too low to account for the lowest fullerene vibration ( $270\text{ cm}^{-1}$ ). Therefore, we can assume that these modes probably belong to MOF since a similar  $\Delta$  was found for all the samples irrespective of the incorporation of fullerene. Therefore, we can propose that fullerene encapsulation prolongates  $T_1$  relaxation time of copper porphyrin MOFs by slowing down direct and Raman processes.

**2.6.2 Phase-memory relaxation time.** The temperature dependence of the electron-spin phase-memory relaxation times,  $T_m$ , of various MOFs is presented in Fig. 6c and S9† for  $g_{\parallel}$  spectral position. At 5 K, the longest  $T_m$  value around 800 ns was detected in  $1.0\text{C}_{60}@Cu_{0.1}\text{-PCN-223}$ . For comparison, the shortest  $T_m$  was observed in  $\text{Cu}_{0.1}\text{-PCN-223}$  (540 ns) whereas  $\text{Cu}_{0.1}\text{-MOF-525}$  featured  $T_m$  of 600 ns (Fig. 6c). Therefore,  $T_m$  is affected by the content of fullerene in the structure giving rise to larger values. The improved values can be ascribed to the partial exclusion of nuclear spin-bearing solvent by the almost nuclear

Table 1 The best-fit parameters to the experimental spin–lattice relaxation rate data according to eqn (2) with a numerical evaluation of the transport integral and referring to  $\text{Cu}_{0.1}\text{-PCN-223}$  (without fullerene),  $0.2\text{C}_{60}@Cu_{0.1}\text{-PCN-223}$  and  $1.0\text{C}_{60}@Cu_{0.1}\text{-PCN-223}$  (with fullerene).  $R^2$  provides information about the goodness of fit of a model

Compound	$g_{\text{position}}$	$a, 1/(\text{K}\mu\text{s})$	$b, 1/(\text{K}^2\mu\text{s})$	$\theta, \text{K}$	$c, 1/\mu\text{s}$	$\Delta, \text{K}$	$R^2$
$\text{Cu}_{0.1}\text{-MOF-525}$	$g_{\parallel}$	$(3.2 \pm 0.3)10^{-5}$	$(4 \pm 2)10^{-5}$	$77 \pm 22$	$7 \pm 4$	$285 \pm 35$	0.999683
$\text{Cu}_{0.1}\text{-MOF-525}$	$g_{\perp}$	$(6. \pm 1)10^{-5}$	$(4 \pm 2)10^{-5}$	$66 \pm 35$	$9 \pm 4$	$292 \pm 31$	0.999429
$\text{Cu}_{0.1}\text{-PCN-223}$	$g_{\parallel}$	$(5.1 \pm 0.3)10^{-5}$	$(3 \pm 1)10^{-5}$	$74 \pm 18$	$5 \pm 2$	$273 \pm 26$	0.99984
$\text{Cu}_{0.1}\text{-PCN-223}$	$g_{\perp}$	$(8.6 \pm 0.7)10^{-5}$	$(4.0 \pm 0.9)10^{-5}$	$67 \pm 19$	$7 \pm 2$	$290 \pm 20$	0.99979
$0.2\text{C}_{60}@Cu_{0.1}\text{-PCN-223}$	$g_{\parallel}$	$(2.9 \pm 0.2)10^{-5}$	$(3.3 \pm 0.7)10^{-5}$	$82 \pm 12$	$4 \pm 2$	$281 \pm 36$	0.999908
$0.2\text{C}_{60}@Cu_{0.1}\text{-PCN-223}$	$g_{\perp}$	$(6.1 \pm 0.9)10^{-5}$	$(3 \pm 1)10^{-5}$	$77 \pm 36$	$5 \pm 2$	$280 \pm 33$	0.999775
$1.0\text{C}_{60}@Cu_{0.1}\text{-PCN-223}$	$g_{\parallel}$	$(3.2 \pm 0.2)10^{-5}$	$(2 \pm 1)10^{-5}$	$94 \pm 40$	$6 \pm 2$	$289 \pm 30$	0.999683
$1.0\text{C}_{60}@Cu_{0.1}\text{-PCN-223}$	$g_{\perp}$	$(6.1 \pm 0.5)10^{-5}$	$(2 \pm 2)10^{-5}$	$94 \pm 44$	$8 \pm 3$	$306 \pm 28$	0.999718



spin-free fullerene guests. Namely,  $^{13}\text{C}$  isotope with nuclear spin  $I = 1/2$  has a natural abundance of 1.07%. The obtained values are of the same order of magnitude as for  $\text{Cu}_{0.1}\text{-PCN-224}$  (ref. 4) and for copper-porphyrin qubits in 2D nanosheets<sup>23</sup> while they are the order-of-magnitude larger compared to the values obtained for  $\text{Zr-Cu-NU-1102}$ .<sup>27</sup> Upon increasing the temperature above 5 K,  $T_m$  exhibited no temperature dependence up to *ca.* 30 K. Here, spectral diffusion as a temperature-independent process can be assumed. Further heating of the samples (40–80 K) revealed a gradual decrease of  $T_m$  according to the Arrhenius type of thermally activated processes with the larger activation energy when the fullerene is present in the MOF structure (Fig. S9†). According to the thorough work of Hadt's group,<sup>51,56</sup> the extensive theoretical work, including ligand field theory and mode-by-mode analyses of various molecular vibrations which might participate in spin decoherence, is required to assign specifically which thermally activated process is taking place, the task beyond here presented study.

**2.6.3 HYSOCORE.** Two-pulse electron Hahn spin-echo decay curves of various MOFs presented strong modulation depths in the coherence time decays reflecting specific nuclear spin environment affecting the copper electron spin relaxation (Fig. S10†). These measurements are equivalent to two-pulse ESEEM experiments which can be extended to the three-pulse version and further to the two-dimensional level, HYSOCORE. Therefore, to help the assignment of the observed modulation patterns, HYSOCORE measurements were performed (Fig. 7a). In the (+,+) quadrant, one can note the signals from the weakly coupled nuclei<sup>57,58</sup> appearing on the diagonal at *ca.* 0.84, 3.7 and 14.4 MHz. The latter peak can be assigned unambiguously to the X-band proton Larmor frequency and corresponds to the hyperfine interaction of copper electron with the remote hydrogen ( $^1\text{H}$ ) nuclei. The other peaks could be assigned to the electron interaction with  $^{14}\text{N}$  and/or  $^{13}\text{C}$  nuclei (Fig. S11†). Specifically,  $^{14}\text{N}$  with nuclear spin  $I = 1$  exhibits non-spherical charge distribution requiring quadrupolar interaction to be considered. The low-frequency peak at 0.84 MHz is close to the cancellation limit when the hyperfine and nuclear Zeeman terms match in one of the electron spin manifolds giving rise to the  $^{14}\text{N}$  quadrupolar transitions.<sup>59,60</sup> For weakly coupled nitrogen, the strongest cross-peaks in the HYSOCORE spectrum generally correlate to double-quantum (DQ) frequencies.<sup>57</sup> Therefore, a diagonal peak at 3.7 MHz might be assigned to the DQ transition of the solvent nitrogen.<sup>57,60,61</sup> However, since  $^{13}\text{C}$  nuclei have Larmor frequency of 3.7 MHz at X-band, they can also contribute<sup>28</sup> and the best way to resolve  $^{13}\text{C}$  from  $^{14}\text{N}$  would be to perform HYSOCORE at higher frequency *e.g.* W-band what is beyond the scope of this work. Furthermore,  $^{14}\text{N}$  can exhibit 2DQ peak at *ca.* 9 MHz<sup>62</sup> as can be noticed in the (-,+) quadrant in Fig. 7a. The assignments pointing to the interaction with nitrogen nuclei refer to remote nitrogens from the solvent (more than 0.4 nm away from the copper electron spin<sup>60</sup>) since directly coordinated ones from the porphyrin ring exhibit large hyperfine coupling which cannot be detected in the HYSOCORE experiment but do affect CW-ESR spectra (Table S1†). As a support for this reasoning one should notice that NMR and FTIR spectra show signals from formamide additives even in

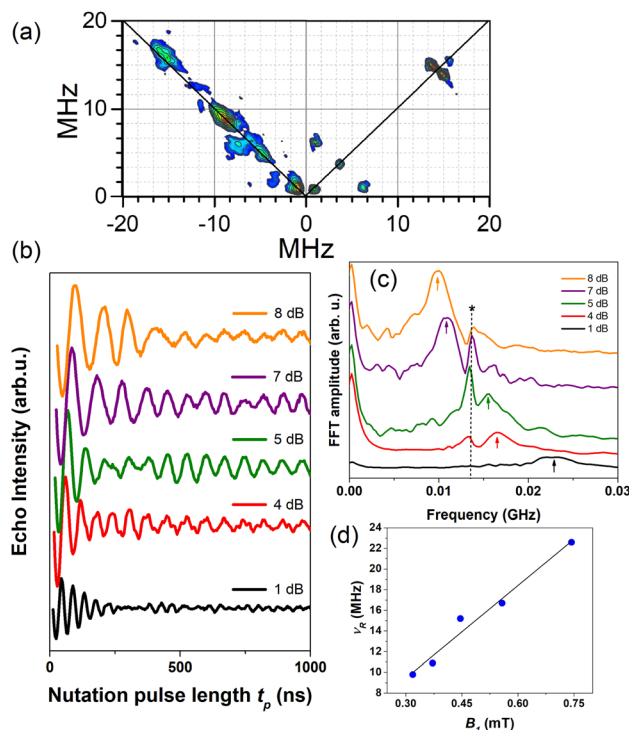


Fig. 7 (a) HYSOCORE performed at 5 K and  $g_{\parallel}$  spectral position for  $1.0\text{C}_{60}@Cu_{0.1}\text{-PCN-223}$  plotted after data processing. (b) Rabi oscillations recorded for  $1.0\text{C}_{60}@Cu_{0.1}\text{-PCN-223}$  at 20 K and  $g_{\parallel}$  spectral position applying various microwave power attenuation. (c) Fast Fourier transform (FFT) of the Rabi oscillations with an asterisk denoting Larmor frequency of proton spins  $\approx 13.5$  MHz while arrows denote Rabi frequencies. (d) Linear dependence of the Rabi frequency,  $\nu_R$ , as a function of the oscillating microwave field,  $B_1$ , calculated according to ref. 63 and 64.

$1.0\text{C}_{60}@Cu_{0.1}\text{-PCN-223}$ , thus, corroborating that formamide solvent molecules are still present in the cavities of PCN-223, likely those present along the crystallographic  $a$  axis.

**2.6.4 Rabi oscillations.** To prove that the samples studied have the potential for application in the field of quantum information processing,<sup>26</sup> the nutation experiments at different microwave powers and 20 K were performed at  $g_{\parallel}$  (Fig. 7b) and  $g_{\perp}$  (Fig. S11†) spectral positions. The interaction between the qubit and the applied microwave field is described by the Rabi frequency, which gives the rate of transition between the ground and excited states. To achieve coherent manipulation between the states, it is a prerequisite for a quantum information processing application to obtain Rabi oscillations with a frequency having linear dependence on the applied microwave field.<sup>65,66</sup> After Fourier transformation of the time domain data, two important types of peaks can be noticed in Fig. 7c. One type is centered at *ca.* 13.5 MHz and shows variable intensity depending on the microwave power. Because these peaks do not present frequency shifts, they can be assigned to coherent electron-proton oscillations. In specific, their intensity reaches a maximum when the Larmor frequency of proton spins matches electron nutation frequency.<sup>10</sup> The second type of peaks represent the nutation frequency peaks,  $\nu_R$ , as they





gradually shift from *ca.* 9 to 23 MHz when the microwave magnetic field increases. It is important to note that these peaks exhibit approximately linear dependence on the microwave field  $B_1$ , as seen in Fig. 7d. This result indicates the possibility of creating an arbitrary superposition of states, thus fulfilling the requirement for possible applications of these types of material in quantum information processing.<sup>65,67</sup>

### 3 Conclusion

In summary, this study shows how the mechanochemical processing accomplished through a robust one-pot ball-milling procedure allowed for control over the ratio of active spin copper(II) carriers and the amount of fullerene  $C_{60}$  guest embedded into the channels of moderately porous porphyrinic zirconium MOFs with twelve-coordinated oxocluster nodes. The use of  $C_{60}$  leads to topological selectivity by governing the formation towards the hard-to-obtain PCN-223 phase, even from reactions that exclusively yield phase-pure cubic MOF-525 polymorph in the absence of fullerene. Here presented experimental evidence points to the possibility of fine-tuning the electron spin relaxation times *via* fullerene content in the MOF cavity, where an increase in  $T_1$  and  $T_m$ , detected in MOF fulleretic hybrids, can be directly related to the ratio of the fullerene guest. It should be emphasized that the increase in the electron spin coherence was observed in the presence of solvent guests without the necessity for MOF activation which usually leads to the collapse of the structure. We propose that fullerene encapsulation prolongates both relaxation times of copper porphyrin MOFs, first through the partial exchange of the nuclear spin-bearing solvents with rigid almost nuclear spin-free fullerenes affecting  $T_m$ , but also through slowing down direct and Raman processes affecting thus  $T_1$ . The nutation experiments presenting linear dependence of the Rabi oscillation on the intensity of the oscillating field indicate the possibility of creating an arbitrary superposition of states, proving that coherent manipulation between the electron spin states in the studied fulleretic MOF hybrids can be achieved. In this way, even the non-activated and densely coordinated zirconium-porphyrin frameworks become viable molecular spin qubit matrices, where the inferior and least porous  $Cu_{0.1}$ -PCN-223 candidate becomes the best qubit performer after the fullerene inclusion. Using similar solid-state strategies, we aim to test how altering the spin carrier species and including fullerene and endometallofullerene derivatives in more porous zirconium-porphyrinic MOFs, such as MOF-525 and well-established six-coordinated framework PCN-224, will affect their spin coherence properties.

### Data availability

All the supporting calculation and experimental data is a part of ESL.†

### Author contributions

The project was conceived and supervised by KU, BK, DŽ, and MK. BK prepared MOF materials and their diluted and

composite phases. NC was involved in the synthesis and characterization of ligands. LV, DŽ, and MK performed CW and pulse ESR measurements and analyses. AK and GM conducted, analyzed, and prepared solid-state NMR spectroscopy. MM carried out and analysed energy dispersive X-ray spectroscopy (EDAX) measurements. SMA and AAP conducted DFT (density functional theory) calculations and molecular dynamics (MD) simulations and wrote part of the DFT study. The initial draft of the manuscript was written by DŽ, BK, MK, and KU. BK and LV prepared the figures and graphical abstract. All authors discussed the results and contributed to the final preparation of the manuscript.

### Conflicts of interest

There are no conflicts to declare.

### Acknowledgements

This research was supported in part by the Croatian Science Foundation through grant IP-2018-01-3168, by the “Research Cooperability” Program of the Croatian Science Foundation funded by the European Union from the European Social Fund under the Operational Programme Efficient Human Resources 2014–2020, through grant PZS-2019-02-4129, and by the DAAD-MZO bilateral project “New generation of magnetic MOF composites based on controllable confinement of selected endofullerenes”. A. K., G. M. and M. M. acknowledge the financial support from the Slovenian Research Agency (research core funding no. P1-0021). A. A. P. thanks Deutsche Forschungsgemeinschaft for financial support (grants PO 1602/6-1 and 1602/11-1). Goran Dražić is acknowledged for the TEM/EDAX mapping measurements.

### Notes and references

- 1 M. Atzori and R. Sessoli, *J. Am. Chem. Soc.*, 2019, **141**, 11339–11352.
- 2 A. Gaita-Ariño, F. Luis, S. Hill and E. Coronado, *Nat. Chem.*, 2019, **11**, 301–309.
- 3 E. Coronado, *Nat. Rev. Mater.*, 2020, **5**, 87–104.
- 4 C.-J. Yu, M. D. Krzyaniak, M. S. Fataftah, M. R. Wasielewski and D. E. Freedman, *Chem. Sci.*, 2019, **10**, 1702–1708.
- 5 M. J. Graham, J. M. Zadrozny, M. S. Fataftah and D. E. Freedman, *Chem. Mater.*, 2017, **29**, 1885–1897.
- 6 T. Andlauer and P. Vogl, *Phys. Rev. B: Condens. Matter Mater. Phys.*, 2009, **79**, 045307–045314.
- 7 S. L. Bayliss, P. Deb, D. W. Laorenza, M. Onizhuk, G. Galli, D. Freedman and D. D. Awschalom, *Phys. Rev. X*, 2022, **12**, 031028–031036.
- 8 H.-C. Zhou, J. R. Long and O. M. Yaghi, *Chem. Rev.*, 2012, **112**, 673–674.
- 9 S. Kitagawa, R. Kitaura and S.-I. Noro, *Angew. Chem., Int. Ed.*, 2004, **43**, 2334–2375.
- 10 T. Yamabayashi, M. Atzori, L. Tesi, G. Cosquer, F. Santanni, M. E. Boulon, E. Morra, S. Benci, R. Torre, M. Chiesa,



- L. Sorace, R. Sessoli and M. Yamashita, *J. Am. Chem. Soc.*, 2018, **140**, 12090–12101.
- 11 S. Kitagawa, *Acc. Chem. Res.*, 2017, **50**, 514–515.
- 12 J. D. Evans, V. Bon, I. Senkowska, H. C. Lee and S. Kaskel, *Nat. Commun.*, 2020, **11**, 2690–2701.
- 13 J. M. Zadrozny, J. Niklas, O. G. Poluektov and D. F. Freedman, *ACS Cent. Sci.*, 2015, **1**, 488–492.
- 14 S. Takahashi, I. S. Tupitsyn, J. van Tol, C. C. Beedle, D. N. Hendrickson and P. C. E. Stamp, *Nature*, 2011, **476**, 76–79.
- 15 M. R. Wasielewski, M. D. E. Forbes, N. L. Frank, K. Kowalski, G. D. Scholes, J. Yuen-Zhou, M. A. Baldo, D. E-Freedman, R. H. Goldsmith, T. G. III, M. L. Kirk, J. K. McCusker, J. P. Ogilvie, D. A. Shultz, S. Stoll and K. B. Whaley, *Nat. Rev. Chem.*, 2020, **4**, 490–504.
- 16 W. Morris, B. Voloskiy, S. Demir, F. Gándara, P. L. McGrier, H. Furukawa, D. Cascio, J. F. Stoddart and O. M. Yaghi, *Inorg. Chem.*, 2012, **51**, 6443–6445.
- 17 D. Feng, W.-C. Chung, Z. Wei, Z.-Y. Gu, H.-L. Jiang, Y.-P. Chen, D. J. Darensbourg and H.-C. Zhou, *J. Am. Chem. Soc.*, 2013, **135**, 17105–17110.
- 18 J. H. Cavka, S. Jakobsen, U. Olsbye, N. Guillou, C. Lamberti, S. Bordiga and K. P. Lillerud, *J. Am. Chem. Soc.*, 2008, **130**, 13850–13851.
- 19 J. E. Mondloch, M. J. Katz, N. Planas, D. Semrouni, L. Gagliardi, J. T. Hupp and O. K. Farha, *Chem. Commun.*, 2014, **50**, 8944–8946.
- 20 X. Liu, N. K. Demir, Z. Wu and K. Li, *J. Am. Chem. Soc.*, 2015, **137**, 6999–7002.
- 21 H. Wu, Y. S. Chua, V. Krungleviciute, M. Tyagi, P. Chen, T. Yildirim and W. Zhou, *J. Am. Chem. Soc.*, 2013, **135**, 10525–10532.
- 22 M. J. Katz, Z. J. Brown, Y. J. Colón, P. W. Siu, K. A. Scheidt, R. Q. Snurr, J. T. Hupp and O. K. Farha, *Chem. Commun.*, 2013, **49**, 9449–9451.
- 23 A. Urtizberea, E. Natividad, P. J. Alonso, M. A. Andrés, I. Gascón, M. Goldmann and O. Roubeau, *Adv. Funct. Mater.*, 2018, **28**, 1801695–1801710.
- 24 Z. Chen, S. L. Hanna, L. R. Redfern, D. Alezi, T. Islamoglu and O. K. Farha, *Coord. Chem. Rev.*, 2019, **386**, 32–49.
- 25 B. Karadeniz, D. Žilić, I. Huskić, L. S. Germann, A. M. Fidelli, S. Muratović, I. Lončarić, M. Etter, R. E. Dinnebier, D. Barišić, N. Cindro, T. Islamoglu, O. K. Farha, T. Friščić and K. Užarević, *J. Am. Chem. Soc.*, 2019, **141**, 19214–19220.
- 26 J. M. Zadrozny, A. T. Gallagher, T. D. Harris and D. F. Freedman, *J. Am. Chem. Soc.*, 2017, **139**, 7089–7094.
- 27 C.-J. Yu, S. von Kugelgen, M. D. Krzaniak, W. Ji, W. R. Dichtel, M. R. Wasielewski and D. E. Freedman, *Chem. Mater.*, 2020, **32**, 10200–10206.
- 28 S. Richert, J. Cremers, H. L. Anderson and C. R. Timmel, *Chem. Sci.*, 2016, **7**, 6952–6960.
- 29 T. Stolar and K. Užarević, *CrystEngComm*, 2020, **22**, 4511–4525.
- 30 X. Zhang, V. Vieru, X. Feng, J.-L. Liu, Z. Zhang, B. Na, W. Shi, B.-W. Wang, A. K. Powell, L. F. Chibotaru, S. Gao, P. Cheng and J. R. Long, *Angew. Chem., Int. Ed.*, 2015, **54**, 9861–9865.
- 31 J. Vallejo, F. R. Fortea-Pérez, E. Pardo, S. Benmansour, I. Castro, J. Krzystek, D. Armentano and J. Cano, *Chem. Sci.*, 2016, **7**, 2286–2293.
- 32 V. Martinez, B. Karadeniz, N. Biliškov, I. Lončarić, S. Muratović, D. Žilić, S. A. Avdoshenko, M. Roslova, A. A. Popov and K. Užarević, *Chem. Mater.*, 2020, **32**, 10628–10640.
- 33 J. L. Woodliffe, R. S. Ferrari, I. Ahmed and A. Laybourn, *Coord. Chem. Rev.*, 2021, **428**, 213578.
- 34 L. Sun, L. Yang, J.-H. Dou, J. Li, G. Skorupskii, M. Mardini, K. O. Tan, T. Chen, C. Sun, J. J. Oppenheim, R. G. Griffin, M. Dincă and T. Rajh, *J. Am. Chem. Soc.*, 2022, **144**, 19008–19016.
- 35 A. R. Mulholland, C. P. Woodward and S. J. Langford, *Chem. Commun.*, 2011, **47**, 1494–1496.
- 36 D.-Y. Zheng, E.-X. Chen, C.-R. Yeab and X.-C. Huang, *J. Mater. Chem. A*, 2019, **7**, 22084–22091.
- 37 J. W. M. Osterrieth, J. Rampersad, D. Madden, N. Rampal, L. Skoric, B. Connolly, M. D. Allendorf, V. Stavila, J. L. Snider, R. Ameloot, J. a. Marreiros, C. Ania, D. Azevedo, E. Vilarrasa-Garcia, B. F. Santos, X.-H. Bu, Z. Chang, H. Bunzen, N. R. Champness, S. L. Griffin, B. Chen, R.-B. Lin, B. Coasne, S. Cohen, J. C. Moreton, Y. J. Colón, L. Chen, R. Clowes, F.-X. Coudert, Y. Cui, B. Hou, D. M. D'Alessandro, P. W. Doheny, M. Dinca, C. Sun, C. Doonan, M. T. Huxley, J. D. Evans, P. Falcaro, R. Ricco, O. Farha, K. B. Idrees, T. Islamoglu, P. Feng, H. Yang, R. S. Forgan, D. Bara, S. Furukawa, E. Sanchez, J. Gascon, S. Telalović, S. K. Ghosh, S. Mukherjee, M. R. Hill, M. M. Sadiq, P. Horcajada, P. Salcedo-Abraira, K. Kaneko, R. Kukobat, J. Kenvin, S. Keskin, S. Kitagawa, K.-i. Otake, R. P. Lively, S. J. A. DeWitt, P. Llewellyn, B. V. Lotsch, S. T. Emmerling, A. M. Pütz, C. Martí-Gastaldo, N. M. Padial, J. García-Martínez, N. Linares, D. MasPOCH and J. A. Suárez, *Adv. Mater.*, 2022, **34**, 2201502–2201524.
- 38 S. M. Shaikh, P. M. Usov, J. Zhu, M. Cai, J. Alatis and A. J. Morris, *Inorg. Chem.*, 2019, **58**, 5145–5153.
- 39 G. Ayoub, B. Karadeniz, A. J. Howarth, O. K. Farha, I. Đilović, L. S. Germann, R. E. Dinnebier, K. Užarević and T. Friščić, *Chem. Mater.*, 2019, **31**, 5494–5501.
- 40 M. Yamashina, Y. Tanaka, R. Lavendomme, T. K. Ronson, M. Pittelkow and J. R. Nitschke, *Nature*, 2019, **574**, 511.
- 41 C. Finazzo, C. Calle, S. Stoll, S. Doorslaer and A. Schweiger, *Phys. Chem. Chem. Phys.*, 2006, **8**, 1942–1953.
- 42 S. Stoll and A. Schweiger, *J. Magn. Reson.*, 2006, **178**, 42–55.
- 43 P. Basu, *J. Chem. Educ.*, 2001, **78**, 666–669.
- 44 K. L. Cunningham, K. M. McNett, R. A. Pierce, K. A. Davis, H. H. Harris, D. M. Falck and D. R. McMillin, *Inorg. Chem.*, 1977, **36**, 608–613.
- 45 V. Gómez-Vidales, A. Borja-Miranda, S. Cortez-Maya, O. Amelines-Sarria, M. Rivera and M. Martínez-García, *Open Chem. J.*, 2016, **3**, 25–34.
- 46 D. Dubois, G. Moninot, W. Kutner, M. T. Jones and K. M. Kadish, *J. Phys. Chem.*, 1992, **96**, 7137–7145.
- 47 K. M. Kadish and M. M. Morrison, *Bioinorg. Chem.*, 1977, **7**, 107–115.



- 48 Y. Zhou, B. E. Bowler, G. R. Eaton and S. S. Eaton, *J. Magn. Reson.*, 1999, **139**, 165–174.
- 49 L. Escalera-Moreno, J. J. Baldoví, A. Gaita-Ariño and E. Coronado, *Chem. Sci.*, 2018, **9**, 3265–3275.
- 50 M. Kveder, D. Merunka, M. Jokić, J. Makarević and B. Rakvin, *Phys. Rev. B: Condens. Matter Mater. Phys.*, 2009, **80**, 052201–052205.
- 51 N. P. Kazmierczak, R. Mirzoyan and R. G. Hadt, *J. Am. Chem. Soc.*, 2021, **143**, 17305–17315.
- 52 J.-L. Du, G. R. Eaton and S. S. Eaton, *J. Magn. Reson., Ser. A*, 1995, **117**, 67–72.
- 53 N. P. Kazmierczak and R. G. Hadt, *J. Am. Chem. Soc.*, 2022, **144**, 20804–20814.
- 54 C. Kittel, *Introduction to Solid State Physics*, John Wiley, New York, Chichester, Brisbane, Toronto, Singapore, 7th edn, 1996.
- 55 B. Huang, Z. Ni, A. Millward, A. McGaughey, C. Uher, M. Kaviani and O. Yaghi, *Int. J. Heat Mass Transfer*, 2007, **50**, 405–411.
- 56 R. Mirzoyan, N. P. Kazmierczak Ryan and R. G. Hadt, *Chem. – Eur. J.*, 2021, **27**, 9482.
- 57 C. Finazzo, C. Calle, S. Stoll, S. Van Doorslaer and A. Schweiger, *Phys. Chem. Chem. Phys.*, 2006, **8**, 1942–1953.
- 58 D. Gourier, O. Delpou, A. Bonduelle, L. Binet, I. Ciofini and H. Vezin, *J. Phys. Chem. B*, 2010, **114**, 3714–3725.
- 59 C. S. Burns, E. Aronoff-Spencer, C. M. Dunham, P. Lario, N. I. Avdievich, W. E. Antholine, M. M. Olmstead, A. Vrielink, G. J. Gerfen, J. Peisach, W. G. Scott and G. L. Millhauser, *Biochemistry*, 2002, **41**, 3991–4001.
- 60 S. Van Doorslaer and E. Vinck, *Phys. Chem. Chem. Phys.*, 2007, **9**, 4620–4638.
- 61 Y. Deligiannakis, M. Louloudi and N. Hadjiliadis, *Coord. Chem. Rev.*, 2000, **204**, 1–112.
- 62 K. I. Silva, B. C. Michael, S. J. Geib and S. Saxena, *J. Phys. Chem. B*, 2014, **118**, 8935–8944.
- 63 G. R. Eaton, S. S. Eaton, R. W. Quine, D. Mitchell, V. Kathirvelu and R. T. Weber, *J. Magn. Reson.*, 2010, **205**, 109–113.
- 64 G. Jeschke, in *Instrumentation and Experimental Setup*, Springer US, Boston, MA, 2007, pp. 17–47.
- 65 J. M. Zadrozny, J. Niklas, O. G. Poluektov and D. F. Freedman, *J. Am. Chem. Soc.*, 2014, **136**, 15841–15844.
- 66 L. Tesi, E. Lucaccini, I. Cimatti, M. Perfetti, M. Mannini, M. Atzori, E. Morra, M. Chiesa, A. Caneschi, L. Sorace and R. Sessoli, *Chem. Sci.*, 2016, **7**, 2074–2083.
- 67 Y.-H. Fang, Z. Liu, Y.-X. Wang, S. Zhou, S.-D. Jiang and S. Gao, *Inorg. Chem. Front.*, 2020, **7**, 3875–3881.

